Schottky-like contact-Induced d-Band Center Shift in $Cu(H_2PO_3)_2$/Boron for Efficient Photocatalytic Hydrogen Evolution

Jixu Han, Jing Xu *, Siming Lan, Xinjie Ning, Mingxia Zheng, Jia Lu

School of Chemistry and Chemical Engineering, Ningxia Key Laboratory of Solar Chemical Conversion Technology, Key Laboratory for Chemical Engineering and Technology, State Ethnic Affairs Commission, North Minzu University, Yinchuan 750021, P.R.China

Corresponding author: Jing_XU@nmu.edu.cn

1. Materials

All of the chemicals and reagents used were of analytical grade (AR).Copper(II) chloride dihydrate ($CuCl_2·2H_2O$, purity ≥99.0%) was procured from Shanghai Guangnuo Chemical Technology Co., Ltd. Eosin Y ($C_{20}H_6Br_4Na_2O_5$) and sodium hypophosphite (NaH_2PO_2, purity 99.0%) were both purchased from Shanghai Aladdin Biochemical Technology Co., Ltd. Boron powder (B, purity ≥98%) was procured from Shanghai Macklin Biochemical Technology Co., Ltd. Barium sulfate ($BaSO_4$, purity ≥98%) was procured from Saen Chemical Technology (Shanghai) Co., Ltd. Anhydrous ethanol (C_2H_6O, purity ≥99.7%) was procured from Shanghai Guangnuo Chemical Technology Co., Ltd. Triethanolamine (TEOA, purity ≥99.5%) was procured from Xuzhou Tianhong Chemical Trading Co., Ltd.

2. Experimental

2.1 Synthesis of $Cu(H_2PO_3)_2$

The $Cu(H_2PO_3)_2$ catalyst was synthesized via a hydrothermal method. The detailed procedure is as follows: 2.63 mmol $(NH_4)_2HPO_4$ and 2.63 mmol $CuCl_2·2H_2O$ were separately dissolved in 80 mL deionized water under magnetic stirring for 2 h until complete dissolution. The mixed solution was transferred to a 100 mL Teflon-lined stainless-steel autoclave, sealed, and heated in an oven at 120 °C for 2 h. After cooling naturally to room temperature, the product was collected by vacuum filtration, washed three times with deionized water and ethanol, and dried at 60 °C under vacuum for 12 h. The resulting blue powder was ground to obtain pure $Cu(H_2PO_3)_2$.

2.2 Synthesis of $Cu(H_2PO_3)_2$/Boron Composite Catalysts

The $Cu(H_2PO_3)_2$/Boron composites were synthesized using a procedure similar to that of

$Cu(H_2PO_3)_2$, with the key modification of adding Boron powder at predefined molar ratios (1:1, 1:3, 1:5, 1:7) to the $(NH_4)_2HPO_4$ and $CuCl_2 \cdot 2H_2O$ mixture during the dissolution step. Subsequent hydrothermal reaction and post-treatment conditions were unchanged. The final products were labeled as $Cu(H_2PO_3)_2$/Boron-1:1, $Cu(H_2PO_3)_2$/Boron-1:3, $Cu(H_2PO_3)_2$/Boron-1:5, and $Cu(H_2PO_3)_2$/Boron-1:7, corresponding to their respective boron incorporation ratios.

2.3 Characterization Techniques

The crystal structures of the synthesized materials were analyzed by X-ray diffraction (XRD, Rigaku SmartLab SE, Cu Kα radiation, 40 kV, 40 mA, 2θ range: 5–80, scan rate: 10 min^{-1}). Morphology and microstructure were examined using transmission electron microscopy (TEM, FEI Tecnai F30, 300 kV accelerating voltage) and scanning electron microscopy (SEM, Thermo Fisher Scientific Apreo 2, Schottky field-emission electron gun, 0.02–30 kV accelerating voltage). Brunauer-Emmett-Teller (BET) surface area and pore size distribution were determined via nitrogen adsorption-desorption isotherms (Micromeritics ASAP 2460). Elemental composition, electronic properties, and chemical states were investigated by X-ray photoelectron spectroscopy (XPS, Thermo Scientific ESCALAB Xi+, Al Kα radiation). Photoluminescence (PL) spectra were recorded on a Horiba FluoroMax-4 spectrofluorometer equipped with 150 W continuous and 20 W pulsed xenon lamps (spectral resolution: 0.2 nm) to evaluate carrier recombination dynamics. UV-visible diffuse reflectance spectra (UV-Vis DRS) were acquired using a PerkinElmer Lambda 750S spectrophotometer with an integrating sphere accessory. Electrochemical impedance spectroscopy (EIS) and Mott-Schottky analyses were conducted on a CHI 660E electrochemical workstation under simulated solar irradiation (300 W xenon lamp, $\lambda \geq 420$ nm cutoff filter).

2.4 Photoelectrochemical and Photoluminescence Measurements

Photocurrent tests were conducted using a CHI 660E electrochemical workstation in a standard three-electrode system. The working electrode was prepared by drop-casting a homogeneous catalyst slurry (5 mg catalyst dispersed in 9 mL ethanol containing 100 μL Nafion solution) onto a 1 × 1 cm^2 fluorine-doped tin oxide (FTO) glass substrate, followed by drying at 60°C for 2 h. A Pt wire and a saturated calomel electrode (SCE) were used as the counter and reference electrodes, respectively. The electrolyte was a 0.2 M Na_2SO_4 aqueous solution. A 300 W xenon lamp with a 420 nm cutoff filter served as the visible-light source. Photocurrent was recorded under intermittent light irradiation (light on/off cycles: 60 s each) at a constant bias of 0 V vs. SCE.

Steady-state PL spectra were acquired on a Horiba FluoroMax-4 spectrofluorometer equipped with a 150 W continuous xenon lamp. The excitation wavelength was set at 420 nm. Samples for PL measurements were prepared by dispersing 2 mg of catalyst in 10 mL of triethanolamine (TEOA) under ultrasonication for 10 min. Time-resolved photoluminescence (TRPL) decay profiles were obtained using a time-correlated single-photon counting (TCSPC) system with a 454 nm pulsed laser diode as the excitation source.

2.5 Photocatalytic Hydrogen Evolution Evaluation

Hydrogen production activities of $Cu(H_2PO_3)_2$/B, pristine $Cu(H_2PO_3)_2$, and boron were evaluated under visible light. A typical procedure involved dispersing 10 mg catalyst, 20 mg eosin Y (EY), and a magnetic stir bar in 30 mL aqueous solution containing 10 vol% triethanolamine (TEOA) within a 60 mL quartz reactor. The reactor was sealed with a 5 mm silicone gasket, ultrasonicated for 4 min to ensure homogeneous dispersion, stirred magnetically at 800 rpm for 4 min, and purged with high-purity N_2 (99.999%) for 4 min to establish an anaerobic environment.

The reaction system was irradiated using a 5 W LED light source ($\lambda \geq 420$ nm) in a PCX50B Discover multi-channel photocatalytic reactor at 25°C with continuous stirring (800 rpm). Gas samples (0.5 mL) were periodically extracted from the headspace using a gas-tight syringe and analyzed by gas chromatography (GC, Agilent 7890B, TCD detector, molecular sieve column) to quantify hydrogen yield.

2.6 Density Functional Theory (DFT) Calculations

First-principles calculations were performed using the CASTEP module in Materials Studio 2020. Crystal models of Boron and $Cu(H_2PO_3)_2$ were geometrically optimized with the Perdew-Burke-Ernzerhof (PBE) functional under the generalized gradient approximation (GGA), employing a 400 eV cutoff energy and a Monkhorst-Pack k-point grid of 10×8×9, with electron-ion interactions modeled through ultrasoft pseudopotentials. Convergence criteria included a self-consistent field (SCF) tolerance of 1×10^{-6} eV atom^{-1} and atomic forces below 0.03 eV Å^{-1}. Electronic structure modulation mechanisms of Boron-doped $Cu(H_2PO_3)_2$ were systematically investigated through band structure analysis, density of states (DOS) calculations, and charge density difference mapping.

3. Results and discussion

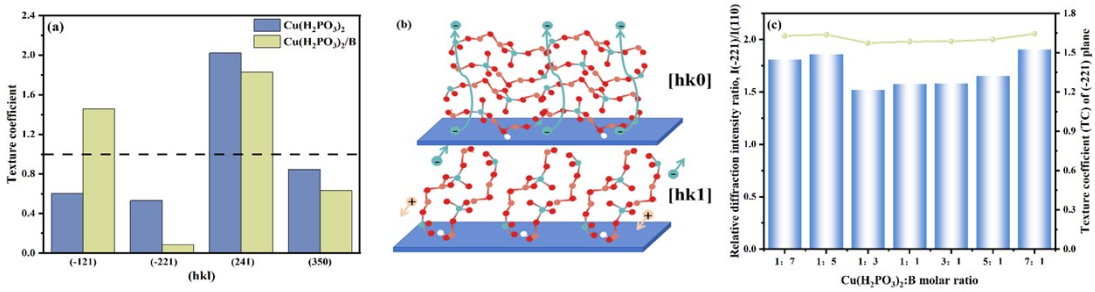

Fig. S1. (a) Texture coefficients of $Cu(H_2PO_3)_2$ and $Cu(H_2PO_3)_2$/B-1:5; (b) Facet-selective growth transition from [hk0]- to [hkl]-oriented configurations; (c) Evolution of the (-221)/(110) intensity ratio and the (-221) texture coefficient with the $Cu(H_2PO_3)_2$: B molar ratio.

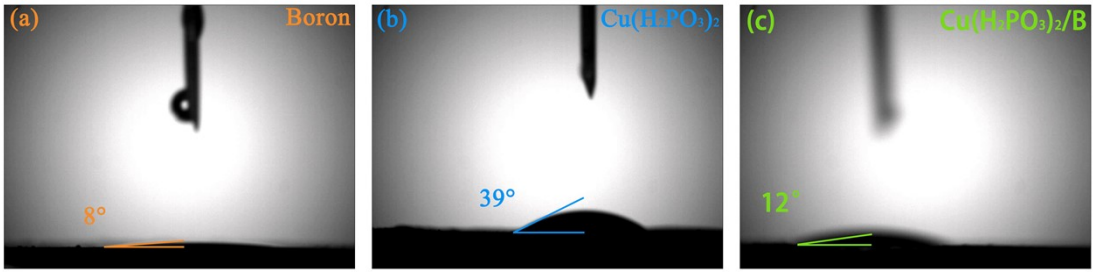

Fig. S2. Surface Hydrophilicity Characterization: (a) Water contact angle of pristine Boron; (b) Water contact angle of pristine $Cu(H_2PO_3)_2$; (c) Water contact angle of $Cu(H_2PO_3)_2$/B-1:5 composite.

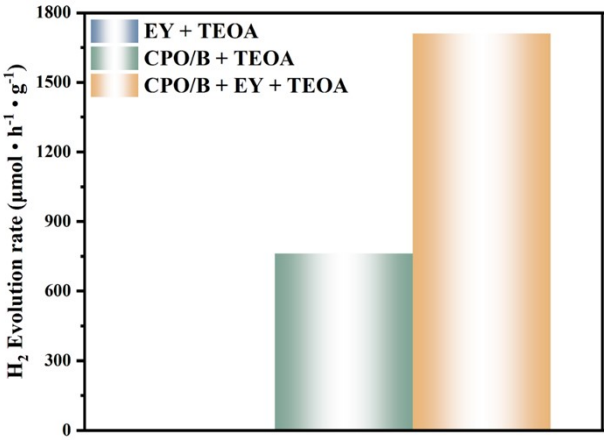

Fig. S3. Control experiments for photocatalytic hydrogen evolution under visible light irradiation: (a) EY + TEOA system without catalyst; (b) $Cu(H_2PO_3)_2$/B-1:5 + TEOA system without EY; (c) $Cu(H_2PO_3)_2$/B-1:5 + EY + TEOA system.

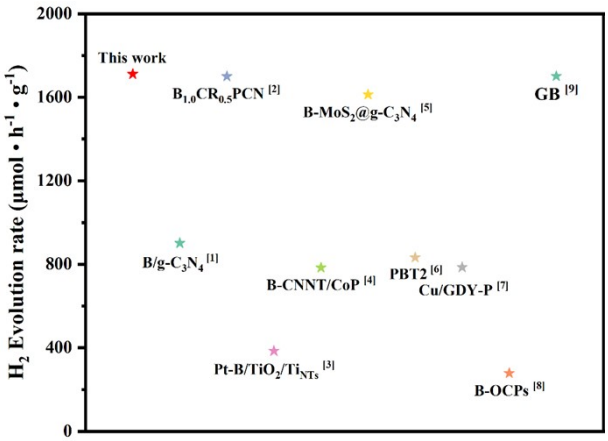

Fig. S4. Comparison of photocatalytic hydrogen evolution performance among representative non-noble metal composite materials reported in recent years [1–9].

References

1 K. Qi, N. Cui, M. Zhang, Y. Ma, G. Wang, Z. Zhao and A. Khataee, Chemosphere, 2021, 272, 129953.

2 Q. Chen, G. Gao, H. Guo, S.-A. Wang, Q. Wang, Y. Fang, X. Hu and R. Duan, Chemical Engineering Journal, 2023, 470, 144199.

3 M. Sun, Y. Jiang, M. Tian, H. Yan, R. Liu and L. Yang, RSC Advances, 2019, 9, 11443–11450.

4 Y. Jiao, Y. Li, J. Wang, Z. He and Z. Li, Journal of Colloid and Interface Science, 2021, 595, 69–77.

5 P. Qiu, Y. An, X. Wang, S. An, X. Zhang, J. Tian and W. Zhu, Chinese Chemical Letters, 2023, 34, 108246.

6 Q. Wei, X. Yao, Q. Zhang, P. Yan, C. Ru, C. Li, C. Tao, W. Wang, D. Han, D. Han, L. Niu, D. Qin and X. Pan, Small, DOI:10.1002/smll.202100132.

7 Y. Wu, X. Wang, T. Wang, P. Zhu and Z. Jin, ACS Applied Nano Materials, 2024, 7, 1950–1959.

8 X. Han, B. Zhang, H. Chen, M. Peng, C. Xue, H. Liu, G. Ma and Y. Ren, Macromolecules, 2025, 58, 1117–1125.

9 N. Gnanaseelan, L. Marasamy, A. Mantilla, S. K. Kamaraj, F. J. Espinosa-Faller and F. Caballero-Briones, International Journal of Hydrogen Energy, 2022, 47, 40905–40919.

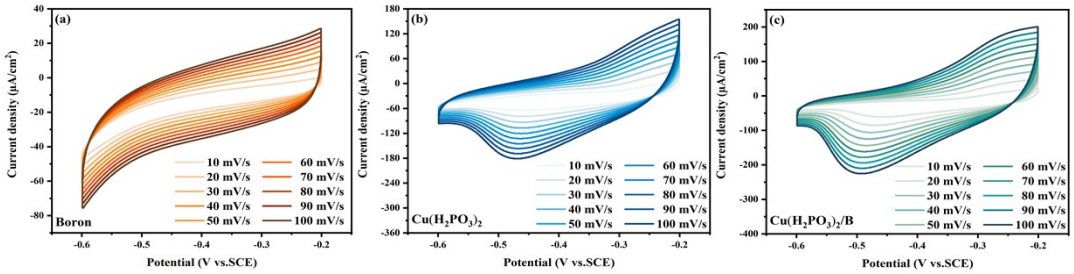

Fig. S5. Cyclic voltammetry (CV) curves of (a) Boron; (b) $Cu(H_2PO_3)_2$; (c) $Cu(H_2PO_3)_2$/B at various scan rates

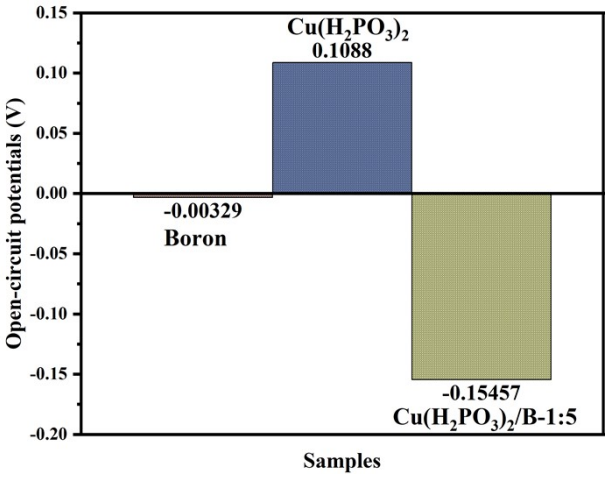

Fig. S6. Open-Circuit Potentials of Boron, $Cu(H_2PO_3)_2$, and $Cu(H_2PO_3)_2$/Boron

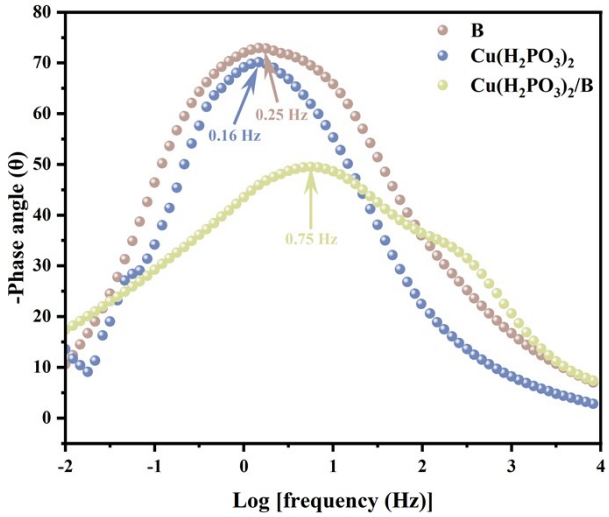

Fig. S7. Boron, $Cu(H_2PO_3)_2$, $Cu(H_2PO_3)_2$/B Bode phase curves

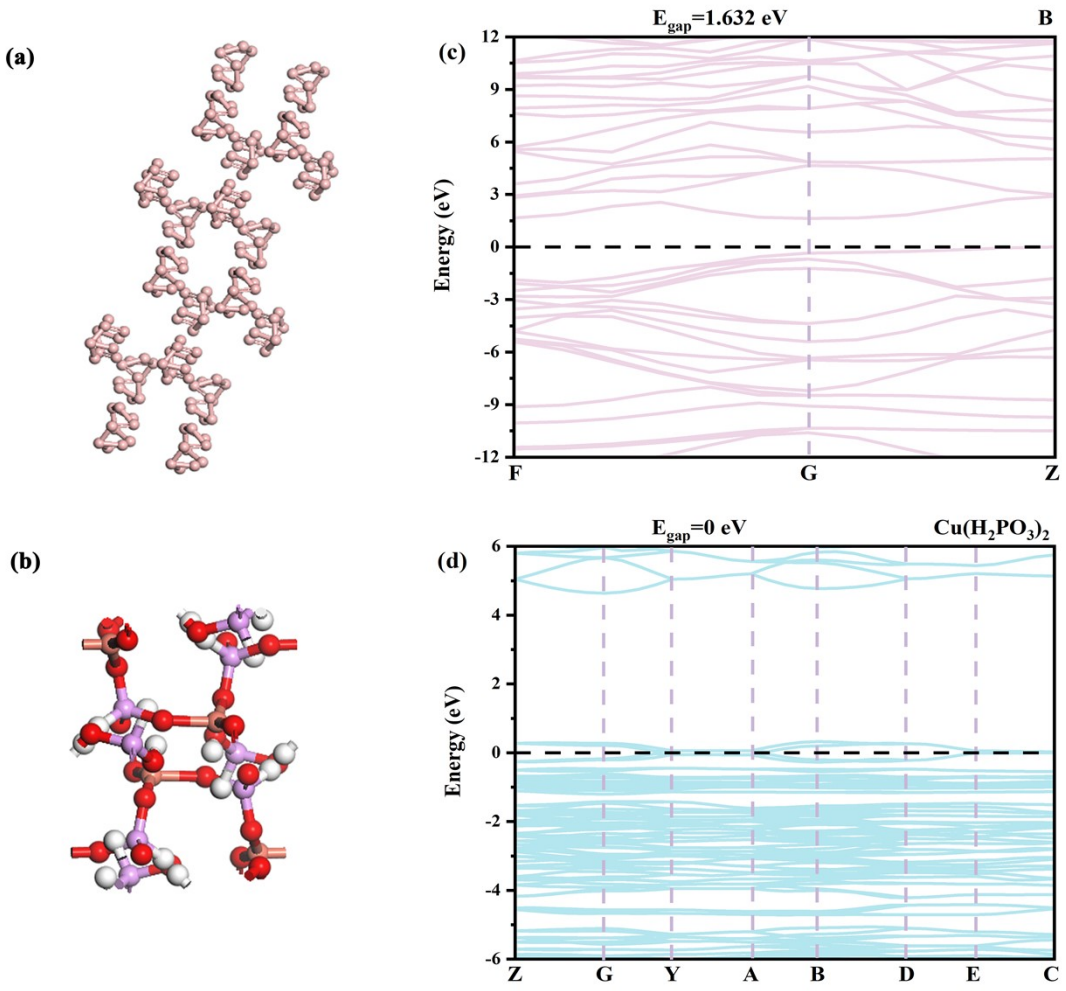

Fig. S8. (a) Monoclinic layered crystal structure of Boron; (b) Two-dimensional coordination framework of copper phosphite; (c) Band structure of boron; (d) Band structure of copper phosphite.

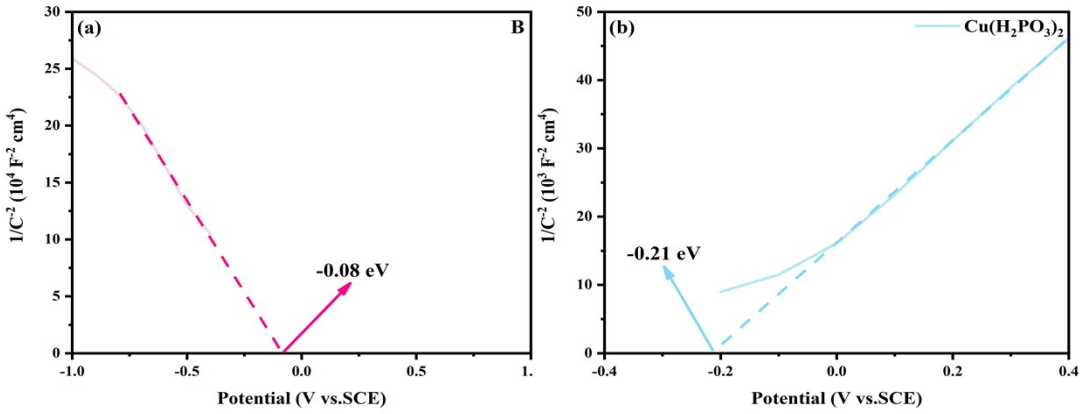

Fig. S9. (a) Boron; (b) $Cu(H_2PO_3)_2$ Mott-Schottky plots

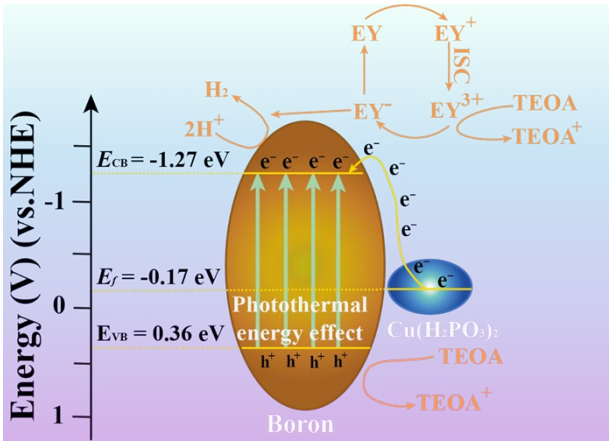

Fig. S10. Schematic diagram of the band alignment and charge transfer pathway.

4. Supporting equations

Bragg's Law and Its Application in XRD Analysis

The crystal lattice parameters and interplanar spacings of the synthesized materials were determined using X-ray diffraction (XRD) analysis. According to Bragg's law, the relationship between the diffraction angle (θ), X-ray wavelength (λ), and interplanar spacing (d) is expressed as:

$$2d \sin\theta = n\lambda \quad \textbf{(S1)}$$

Where n is the diffraction order (an integer), λ is the wavelength of the incident X-rays (0.15418 nm for Cu Kα radiation), d is the interplanar spacing, and θ is the Bragg angle. This equation underpins the interpretation of XRD peak shifts observed in the $Cu(H_2PO_3)_2$/B composites.

Carrier Lifetime Calculation Using Bode Phase Analysis

The carrier lifetime of the sample was calculated from the corresponding frequencies of the characteristic peaks in the Bode phase curves using the following equation:

$$\tau e = \frac{1}{2\pi f max} \quad \textbf{(S2)}$$

where τe is the carrier lifetime and $f$max is the frequency corresponding to the maximum peak near the low-frequency region.

Crystallization Kinetics and Morphological Control via the Thomson-Gibbs Equation

The relationship between supersaturation, surface energy, and crystallite size during hydrothermal growth was analyzed using the Thomson-Gibbs equation:

$$\Delta\mu = \mu_1 - \mu_C = \frac{2\sigma\upsilon}{h} \quad \textbf{(S3)}$$

where Δμ is the chemical potential difference driving crystallization, σ is the surface energy of the crystallographic plane, υ is the molar volume of the growth unit, and h represents the critical dimension (e.g., step height or interplanar spacing). Higher supersaturation (Δμ) reduces the critical nucleus size (h), promoting rapid nucleation and anisotropic growth.

Determination of Bandgap Energy (E_g) via Optical Absorption Analysis

The optical bandgap (E_g) of the semiconductor materials was calculated using the Tauc relation derived from UV-vis diffuse reflectance spectroscopy (DRS) data. For direct and indirect bandgap semiconductors, the relationship between the absorption coefficient (α), photon energy (hν), and E_g is expressed as:

Direct Bandgap Semiconductor:

$$(\alpha h\nu)^2 = A(h\nu - E_g) \quad \textbf{(S4)}$$

Indirect Bandgap Semiconductor:

$$(\alpha h\nu)^{1/2} = A(h\nu - E_g) \quad \textbf{(S5)}$$

Here, α is the absorption coefficient (cm^{-1}), hν is the photon energy (h: Planck's constant, ν: light frequency), and A is a proportionality constant. For direct bandgap materials, A is typically 1/2, while for indirect bandgap materials, A=2, reflects differences in electronic transition mechanisms.

Tafel Equation for Hydrogen Evolution Reaction Kinetics Analysis

The relationship between overpotential (η) and current density (j) in hydrogen evolution reaction (HER) kinetics was quantified using the Tafel equation:

$$\eta = a + b \cdot \log j \quad \textbf{(S6)}$$

Here,η is the overpotential (V vs. RHE), a is a constant related to the exchange current density (V), b is the Tafel slope ($V \cdot dec^{-1}$), reflecting the reaction mechanism, j is the current density ($mA \cdot cm^{-2}$).

The logarithmic dependence of η on j allows extraction of the Tafel slope (b) from linear fitting of the polarization curve. A lower Tafel slope indicates faster HER kinetics, as less additional potential is required to drive a tenfold increase in current density. This analysis standardizes the evaluation of electrocatalytic activity under HER conditions.

Determination of Flat-Band Potential and Semiconductor Type via Mott-Schottky Analysis

The flat-band potential (V_{fb}) and semiconductor type (n-type or p-type) were determined using Mott-Schottky analysis. The relationship between the space charge capacitance (C) and applied bias (V) is expressed as:

$$\frac{1}{C^2} = \frac{2}{Ne\varepsilon\varepsilon_0}(E - E_{fb} - \frac{KT}{e}) \quad \textbf{(S7)}$$

where C is the space charge capacitance, N is the carrier density, e is the unit charge, ε0 and ε are the vacuum and relative permittivity, respectively, E is the applied bias voltage, K is the Boltzmann constant, and T is the absolute temperature.

Potential Conversion between RHE and SCE via the Nernst Equation

The conversion of electrode potentials measured versus the saturated calomel electrode (SCE) to the reversible hydrogen electrode (RHE) scale was performed using the Nernst equation:

$$E_{RHE} = E_{SCE} + 0.0591 \times pH + 0.244 \quad \textbf{(S8)}$$

where E_{SCE} is the applied potential relative to SCE, and the electrolyte (0.2 M Na_2SO_4) at 25°C had a pH of 7. The term 0.244V accounts for the standard potential difference between SCE and the standard hydrogen electrode (SHE). This conversion ensures accurate comparison of electrochemical data under standardized hydrogen evolution reaction (HER) conditions.

Gibbs Free Energy Calculation

The Gibbs free energy of hydrogen adsorption (ΔG_{H^*}) was calculated using the following equation:

$$\Delta G_{H^*} = \Delta E_{H^*} + \Delta E_{ZPE} - T\Delta S \quad \textbf{(S9)}$$

Where $\Delta E_{H^*}$is the hydrogen adsorption energy, ΔE_{ZPE} is the zero-point energy correction, TΔS is the entropy contribution at temperature T, and ΔSrepresents the entropy change between the adsorbed H^* species and gaseous H_2.

Hydrogen Adsorption Energy Calculation

The hydrogen adsorption energy (ΔE_{H^*}) was calculated using the following equation:

$$\Delta E_{H^*} = E_{H^*} - E - 1/2E_{H2} \quad \textbf{(S10)}$$

Where E is the total energy of the clean substrate, E_{H2} is the total energy of a hydrogen molecule in the gas phase, and E_{H^*} is the total energy of the substrate with an adsorbed hydrogen atom (H^*).

d-Band Center Calculation

The d-band center (ε_d) was calculated using the following equation:

$$\varepsilon_d = \frac{\int_{-\infty}^{\infty} n_d(\varepsilon)\varepsilon d\varepsilon}{\int_{-\infty}^{\infty} n_d(\varepsilon) d\varepsilon} \quad \textbf{(S11)}$$

Where ε is the energy level (relative to the Fermi level), and n_d (ε) is the d-projected density of states.